

Dynamic organ modeling for minimally-invasive cardiac surgery

Stanislaw Szpala¹, Marcin Wierzbicki¹³, Gerard Guiraudon²³⁴, Terry Peters¹²³

¹Robarts Research Institute, ²Lawson Health Research Institute, ³University of Western Ontario,

⁴Canadian Surgical Technologies and Advanced Robotics (C-STAR), London, Ontario, Canada

{sszpala, mwierz, tpeters}@imaging.robarts.ca

Keywords: Virtual endoscopy, minimally-invasive cardiac surgery, image guidance, image warping.

ABSTRACT

While most currently available minimally invasive robotically assisted cardiac surgical systems do not employ 3D image guidance, such support can be generated using pre operative images such as CT. Previously we demonstrated a virtual model of the thorax with simulated surgical instruments, and a pulsating virtual model of the coronary arteries. In this paper we report the overlay of optical endoscopic images of a beating heart phantom with CT-based dynamic volumetric images of the phantom. Spatial matching is obtained through optical tracking of the endoscope and of the phantom, while time synchronization of the display of the model utilizes ECG gating. The spatial accuracy between the optical and virtual images varies from about 0.8 mm to -2.6 mm, while the time discrepancy depends on the frame-rate at which the virtual model is refreshed, and is typically 50-100 ms. Although the CT-based dynamic images are sufficient for animation of the model, artefacts associated with the image registration prevent seamless animation. Instead, to reconstruct the various phases of heart pulsation, we used a high-quality semi-static image of the diastolic phase of the phantom, and warped it to match the CT-based images corresponding to other phases of the heart pulsation.

1. INTRODUCTION

Patient trauma and incision sizes during surgery have progressively been reduced by the medical community, especially after the first laparoscopic cholecystectomy [1] in 1985, but the concept of minimally invasive surgery was applied to coronary artery bypass graft (CABG) procedure almost thirteen years later. Stevenson *et al.* [2] performed the first totally endoscopic CABG on animals in 1998. The next year Loulmet *et al.* [3] and Mohr *et al.* [4] independently reported the procedure performed on humans, while Kiaii *et al.* [5] performed the first minimally invasive robotic coronary artery bypass (MIRCAB). Such a long delay was partially caused by slow development of reliable telemanipulators, with ARTEMIS (1992) being one of the first capable of operation in six degrees of freedom. The Zeus and da Vinci telerobotic devices are currently the most commonly used systems in surgical practice [6]. It soon became apparent that limited view of optical endoscopes, the primary intra-operative monitoring tool, as well as inaccessibility of visually-obstructed organs, could be complemented with a virtual environment generated from preoperative data obtained from imaging modalities like three-dimensional (3D) computerized tomography (CT) or MRI. Vining *et al.* [7] demonstrated that 3D reconstruction of CT images was useful in examining the tracheobronchial tree, while Gulbins *et al.* [8] showed that 3D imaging was invaluable in the planning of minimally invasive CABG.

We have developed at our institution a virtual cardiac surgical platform using pre- and intra-operative imaging modalities: Chiu *et al.* [9] demonstrated an overlay of endoscopic images with CT-reconstructed thorax phantom, and Lehmann *et al.* [10][11] developed virtual animated coronary arteries derived from 2D bi-plane angiograms. Recently, we superposed tracked-endoscope images with CT-derived organ models in neurosurgical context [12], while in other work, Shahidi *et al.* [13] applied similar methodology to clinical cases. Mourguess *et al.* [14] developed an image-based refinement procedure for orienting a stereoscopic endoscope with respect to an animal heart.

In this paper we present our results involving the fusion of CT-based preoperative images of a beating heart phantom with images from an endoscope that is optically tracked with respect to the phantom. We demonstrate real-time fusion of the endoscopic images with the virtual environment that is robust with respect to the position and the orientation of the endoscope and the phantom, as well as the phase of the cardiac cycle of the heart phantom. Building on earlier work [15], we report further enhancements to the system, including improved tracking of the endoscope pose (position and orientation), and a new method of animation of the virtual model of the beating heart. The new animation warps the 3D image of the diastolic phase to the images of other phases of the cardiac cycle, and provides visually superior results when compared to the previously published animation based on direct images from the cardiac cycle. This is a continuation of the development of the virtual cardiac surgical planning (VCSP) [10] environment, and part of an effort to provide comprehensive imaging support to an intraoperative cardiac surgical assistance environment that employs a telemanipulation system. Our long-term objectives are similar to those of Adhami and Coste-Manière [16].

The significance of this project relates to the fact that minimally invasive surgery is hampered by the lack of adequate image guidance at both the procedure-planning and guidance phases, and this project attempts to relate the endoscopic image to the context of the entire organ through dynamic fusion. This approach also serves to provide a virtual representation of aspects of the organ not seen by the endoscope.

2. METHODS

2.1. Description of the system

In this study, we used a beating heart phantom, section 2.2.1., which simulates the environment of a human heart placed in the thorax, see Figure 1. The phantom was viewed with a standard endoscope, section 2.2.2. A virtual model of the beating heart phantom was constructed based on 3D-CT images collected during a “cardiac cycle”. Fourteen images (representing separate phases of the cardiac cycle) were retrieved, and used to model the movement of the phantom surface. The actual virtual images of the phantom during the cardiac cycle were obtained by extracting a description of the cardiac motion from the CT scans obtained throughout the cardiac cycle, and using this information to warp a high-quality “diastolic phase” image progressively throughout the cardiac cycle, section 2.3.2. Such images of

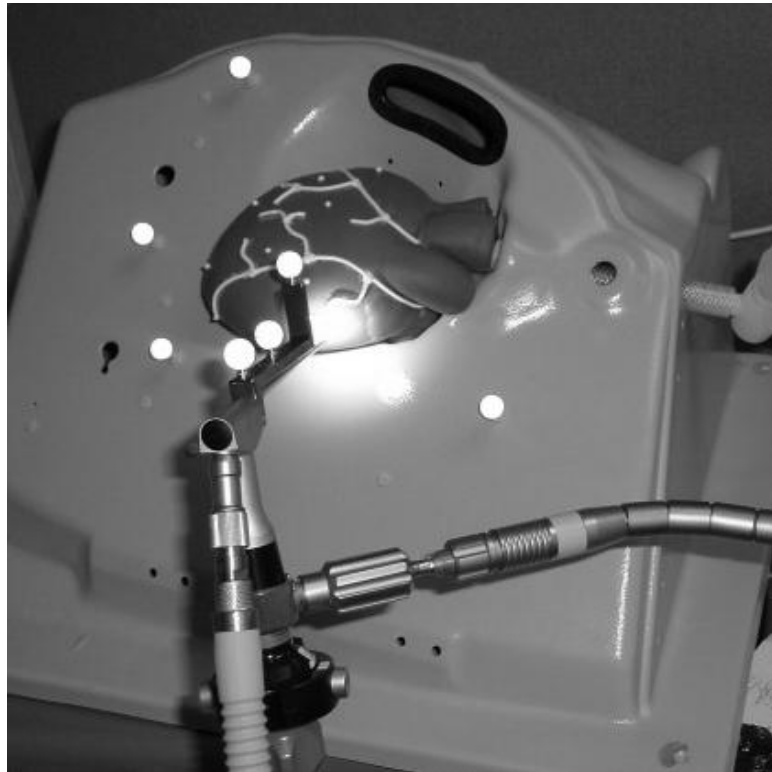


Fig. 1. The beating heart phantom in the model thorax (shown with ribs and skin removed) is visualized with an optically tracked (bright retroreflective Polaris balls) endoscope.

the phantom were displayed in the virtual scene to provide animated representation of the virtual model of the phantom. The animation was time synchronized with the beating of the phantom by triggering the display cycle with an ECG-like signal generated by the phantom controller. The phantom was tracked optically (see section 2.2.4.), and the tracking information was used to position the virtual phantom in the virtual scene. The rendering camera was placed in the location and orientation determined with the tracking probe attached to the endoscope. The images from the endoscope were displayed on the half-transparent plane placed in front of the rendering camera. The endoscope images were

corrected for barrel distortion. The virtual scene was continuously updated to reflect the movement of the endoscope or the heart phantom, and the beating of the phantom.

2.2. Components

2.2.1. Heart phantom

For our validation experiments we employed an inflating / deflating heart phantom (Limbs & Things Limited, Bristol, UK, model 40503), where the volume was adjusted using the supplied air pump and the controller. The controller was modified to provide an “r-wave” equivalent phase synchronization signal generated at the effective “diastolic” phase of the motion. The signal (200 ms TTL pulse) was triggered by a magnetic switch that closes on a preselected phase of the air pump, and was fed to the computer via the parallel port. To uniquely correlate the volume of the phantom with the phase of the air pump, a homing procedure was designed: the piston of the pump would move until detection of the synchronization signal, and then the pressure in the system was adjusted to 15 ± 1 mmHg (measured with a digital blood pressure monitor).

Coronary vessels were replicated using insulated flexible copper (stranded) wires (selected for optimum visibility in CT scans) that were glued to the phantom with silicone. 2 mm in diameter white-painted ball-bearings were glued to the phantom surface for validation purposes.

2.2.2. Endoscope

The endoscopic images were provided by an Aesculap (Melsungen, Germany) 0° fixed focal length neurosurgical endoscope. The barrel distortion of the lens was removed using correction software (see section 2.3.1.), and the calibration was performed in a manner similar to that employed by Shahidi *et al.* [12].

2.2.3. Virtual model of the beating heart phantom

The dynamic images needed to construct the virtual model of the beating phantom were acquired using a 3D-CT scanner (GE Medical System LightSpeed helical, 8 slices of 1.25 mm thickness, 0.5 s rotational period, 120 kV / 300 mA). Because of the symmetry of the inflating / deflating motion in our model, only the first half of the cardiac cycle was reconstructed (7 phases lasting 7 % of the period each). The remaining 7 phases were constructed from the first half period, assuming a cosine time dependence. To compensate for missing the 1 % of the cycle in the reconstructed 7 phases, the 8-th phase was started at 51 % of the period. The warping algorithm used to generate the images used in the animation of the virtual beating phantom from those acquired by the CT scanner is described in section 2.3.2.

2.2.4. Tracking

A Polaris optical tracking system (Northern Digital Inc., Waterloo, ON, Canada) was used to track the pose of both the endoscope and the heart phantom. For endoscope tracking, a custom-made tracking probe consisting of three retroreflective balls was mounted onto the endoscope, while for the phantom tracking, another set of three retroreflective balls was attached rigidly to the phantom holder. Since the phantom may be placed in a receptacle in the phantom holder in a reproducible manner, only the casing of the phantom holder needs to be tracked in order to establish the pose of the heart phantom.

2.3. Software

2.3.1. Program description

The program controlling the system was written in Python 2.1, and makes extensive use of classes from freeware software: VTK 4.1 (www.vtk.org) and Atamai 1.0 (www.Atamai.com). It runs under Windows 2000, on an AMD Athlon MP 1800+ computer, together with ASUS V8200 Series v31.40b display adapter. A Matrox Corona video digitizer was used to digitize the analog signal from the video camera attached to the endoscope.

The program displays a semi-opaque endoscope view overlaid with the virtual image of the heart phantom, as described in section 2.1. The relative pose of the endoscope with respect to the phantom is calculated based on the

information from the tracking probes attached to the endoscope and the phantom. The 4×4 pose matrices are updated every 20 ms. To minimize jitter in the coordinates returned by the Polaris system, the pose matrices are quasi-averaged (i.e. the translation components and the Euler angles are averaged up to 80 consecutive matrices, followed by orthogonalization of the rotation sub matrix) when the endoscope is not moving.

The virtual 3D scene was constructed as follows: The rendering camera was placed at the location in the virtual scene corresponding to the location in the real space of the focal point of the tracked endoscope. Next, a rectangular plane was placed in front of the rendering camera, and the endoscopic image was displayed on it. The endoscopic image was radially warped to remove the barrel distortion of the lens. Although the distortion coefficients were determined in a separate calibration procedure, the image deformation was performed in a near-real time rate of 14 Hz through texture mapping within the graphic card [17]. Finally, the time-synchronized isosurfaces of the preoperative images of the beating heart phantom were added (section 2.2.3.). The isosurfaces were generated using the marching cubes algorithm, and refined with the warping algorithm (section 2.3.2.). The isosurfaces of the heart phantom were transformed from 3D coordinates of the CT scanner, to 3D real-space coordinates, and the transform was determined from the CT-scan coordinates of three markers of known geometrical positions in real space.

2.3.2. Warping algorithm for animation of the virtual model of the beating heart phantom

We animated the static virtual model of the phantom using dynamic information obtained by our automatic, non-linear, image registration algorithm [18]. In this approach, the image used to create the static model was treated as the reference, and was registered to all the remaining image frames. The resulting non-linear transformations were then applied to the static surface model in order to deform it into the different time frames. This “parallel” registration approach ensures that there is only one mapping between the reference image and the frame of interest, avoiding the problem of error accumulation possible if the reference frame was deformed serially from frame to frame.

The actual registration algorithm used to derive the non-linear transformation between two image frames is an entirely automatic, intensity-based approach in a free form deformation (FFD) scheme. In this framework, both the source and target images are overlaid with a structured grid of control points (nodes). Each node is associated with a 3D region of source and target image space surrounding it. A non-zero displacement vector can then be defined for a given node to model the local deformation in this area of the source image. The actual lengths and directions of the individual vectors are chosen using a downhill simplex optimization algorithm [19], with each node being treated independently in sequence. For a given vector x,y,z , the optimization algorithm minimizes the following cost function:

$$\text{cost}(x, y, z) = \sum_V |I_{SO}(x, y, z) - I_{TA}| + \alpha \cdot BE(x, y, z), \quad (1)$$

where $I_{SO}(x,y,z)$ are the intensities in the source image data following a translation by (x,y,z) , I_{TA} are the original intensities of the target image, V is the volume of the source and target data under consideration (usually equal to grid spacing), and BE is the bending energy associated with the current choice of vector (controlled by the user defined parameter α). The first term of equation 1 is the sum of absolute difference of intensities (SAD), a simple and computationally efficient similarity measure used previously in serial image registration. The second term is the 3D equivalent of the thin-plate spline bending energy, responsible for ensuring that the calculated transformation is smooth [20].

To avoid local minima, we employ a multi-resolution grid approach when registering two images. The optimization usually takes place at grid resolutions of 40^3 mm^3 , to 20^3 mm^3 , and finally 10^3 mm^3 . Between the computational stages, the grid is interpolated linearly for improved efficiency.

2.3.3. Calibration software

For proper construction of the virtual scene, the transform between the coordinates of the optical endoscope (origin at the focal point, x-axis along the optical axis of the lens, and z-axis vertical on the computer screen) and the Polaris tracking probe attached to it needs to be known. Although this transform can be established based on geometrical considerations, it can be refined using the following stand-alone procedure (software written in Microsoft Visual C++ 6.0, using VTK 4.1 classes). The procedure consists of non-linear least-squares minimization of the error function defined as the cumulative screen distance between the endoscopic-view and the calculated screen positions of markers of known real-space location. The summation was based on multiple snapshots of four markers collected from various endoscope poses. Since the transform was needed to calculate the screen coordinates of the virtual markers

(defined by 3 translation and 3 angular coefficients), the required transform is its value at the minimum of the error function. Additionally, the calculation requires entering the viewing angle of the camera, and its value was also optimized by this minimization routine. Because of the ease with which their image coordinates can be calculated, the markers used in this procedure were Polaris retroreflective balls attached to the phantom casing.

3. RESULTS

This section contains analysis of the performance of selected components of the system, and validation of the overall system under static and dynamic conditions.

3.1. Transform from tracking coordinates to the coordinates of the optical endoscope

Example snapshots (Figure 2) before and after applying the correction transform (section 2.3.3.) demonstrate the improvement of the overlay between the endoscope image of a test setup and its virtual equivalent. For validation purposes 16 additional snapshots pairs were collected from various endoscope poses for the total of 44 data points. The errors were expressed in terms of “projected errors”, defined as the vector between the investigated point in real space and its image in the endoscope plane, after conceptually shifting the endoscopic plane along the endoscope axis to intercept the investigated point. Histograms of the “projected errors” were calculated before and after applying the correction transform (Figure 3). Markers other than those used in the minimization routine were employed in this validation. The mean projected error of 3.5 mm was reduced to 0.88 mm with the correction transform.



Fig. 2. Proper alignment of the markers in the endoscopic view with their virtual counterparts is achieved through applying the correction transform (right). The corresponding uncorrected image is shown on the left. Each of the three spherical markers visible in the pictures is 11.5 mm in diameter. While the virtual markers are shifted from the locations in the optical locations in the uncorrected image, the shift is reduced in the corrected image.

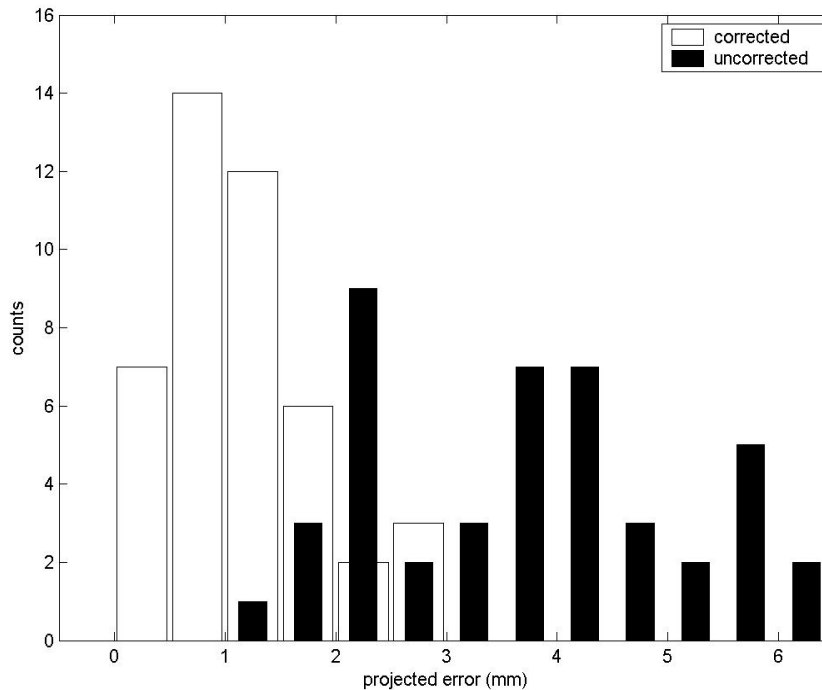


Fig. 3. The histogram of projected errors after applying the correction transform is shifted towards lower values with respect to the uncorrected data. The mean value of the projected error is reduced from 3.5 mm to 0.88 mm.

3.2. Static validation

Static validation of the setup, i.e. for a non-beating phantom, was performed prior to the dynamic (beating phantom) testing. An example snapshot of the rendering pane containing the non-beating phantom with attached coronary arteries is shown in Figure 4(a). The image contains a semi-transparent endoscopic image (also shown in Figure 4(b)) and the virtual model of the phantom (Figure 4(c)).

The static registration errors were determined using fiducial markers (steel ball-bearings) mounted on a rigid wooden model of the heart instead of the flexible heart phantom. The true 3D coordinates of the markers were derived from a separate 3D-CT scan. Since we only have a 2D view of the scene, it is impractical to calculate the true target registration errors (TRE), i.e. the distance between a point in 3D space and its equivalent in “endoscope space”. Instead, we calculated a 2D equivalent of TRE, the “projected error” as defined in section 3.1. The length of the projected error vector is expressed in millimetres, and serves as an estimate of the projected localization of an organ in real space based on its endoscope image overlaid with the virtual equivalent of that organ.

The projected errors were examined for variety of endoscope poses with respect to the static heart phantom. The average absolute value of the projected error for 100 data points was 0.50 ± 0.33 mm.

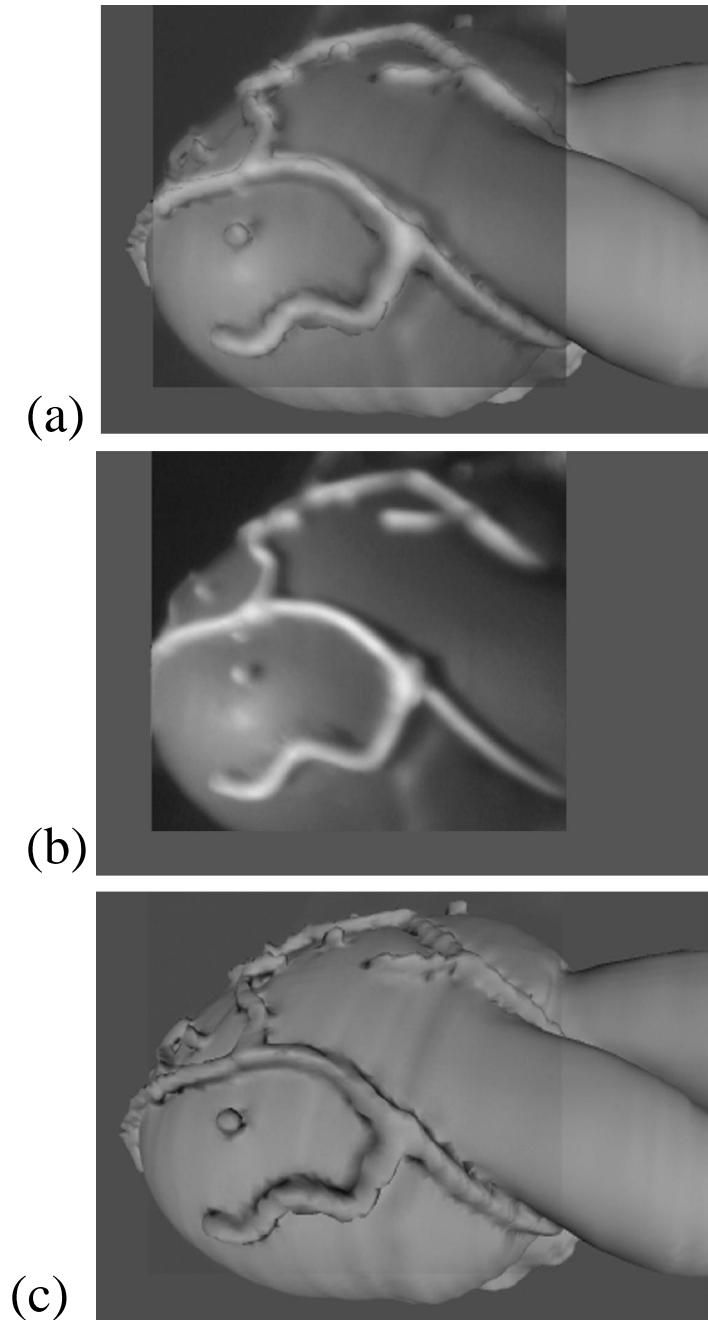


Fig. 4. The overlay (a) of the optical (b) and the virtual (c) demonstrated on a non-beating phantom.

3.3. Validation on a beating phantom

In this section we validate the precision of the overlap of the optical and virtual images of the pulsating heart phantom. The snapshots of the rendering window were saved and analyzed for all 14 phases of the cardiac cycle (for the heart rate of 42 bpm). The snapshots of the first half of the cycle are shown in Figure 5. The complete set of snapshots could not be saved during a single cardiac cycle due to the computer lock-up during the window-saving process

(~0.2 s). Therefore, only one snapshot was collected during a cycle, and the snapshot of the next phase of the cardiac cycle were collected from a new cycle, after receiving the next ECG-like synchronization signal (triggering the heart-display cycle). The opacity of the endoscopic view (displayed as a rectangle in the images below) was set to 65 % to allow simultaneous viewing of the optical and virtual images.

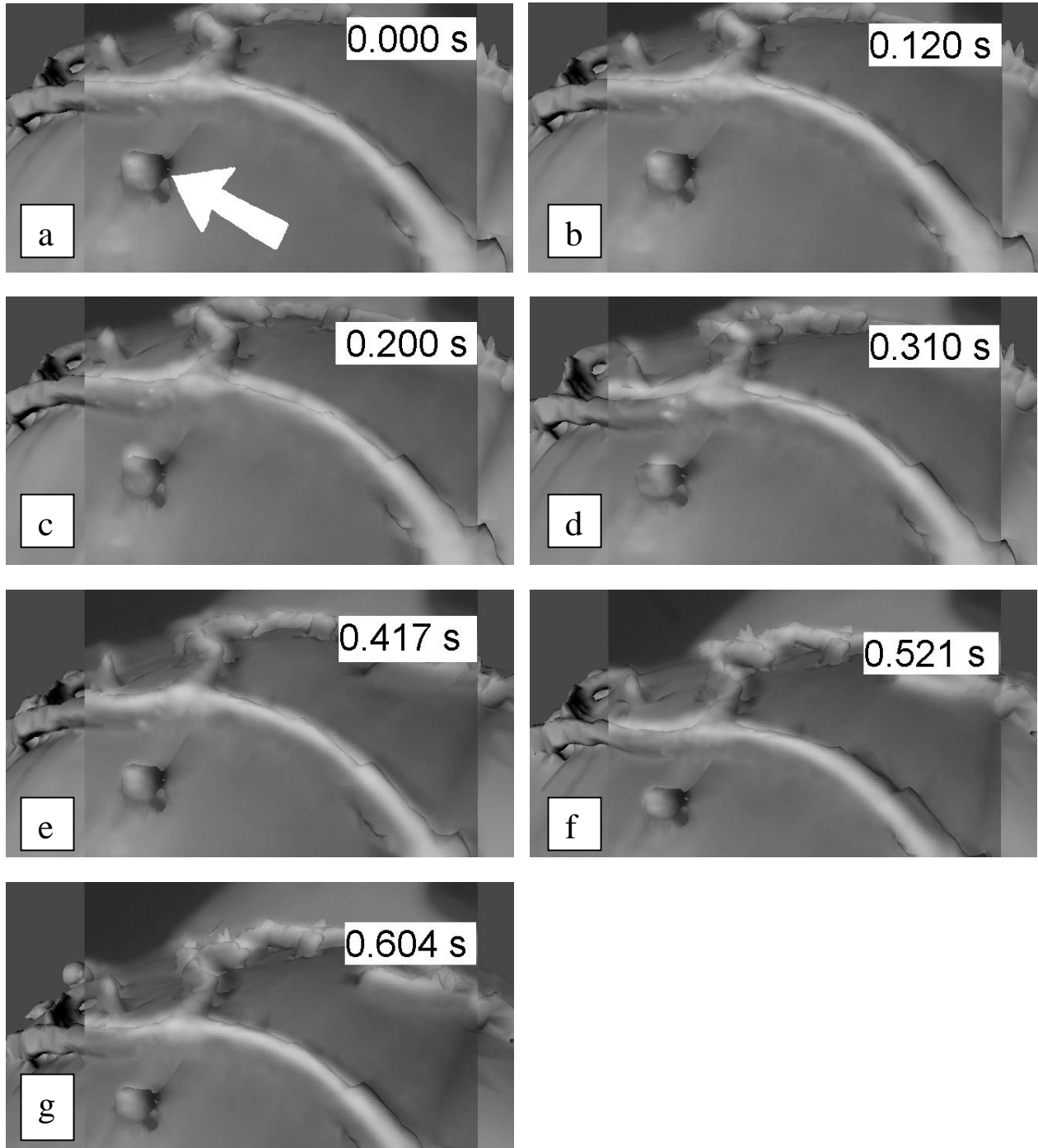


Fig. 5. Snapshots of the first half of the cardiac cycle. Time elapsed from the beginning of the cycle is shown. The (darker) rectangular area at the center of each snapshot marks the view of the optical endoscope. The white arrow points at the marker used for validation.

Figure 5 demonstrates that satisfactory overlap of the optical and virtual images is achievable at all phases of the cardiac cycle. The coronary vessels and the fiducial markers are represented appropriately in all phases. This dramatic improvement of the feature quality in the virtual images, as opposed to that presented in our preliminary work [15], is due to the use of the warping algorithm to update a single model to represent all phases of the cardiac cycle, rather than constructing a new model from the sequence of (sometimes highly artefact-ridden) dynamic CT images. These low-quality images nevertheless contain sufficient information to describe the heart motion throughout the cardiac cycle.

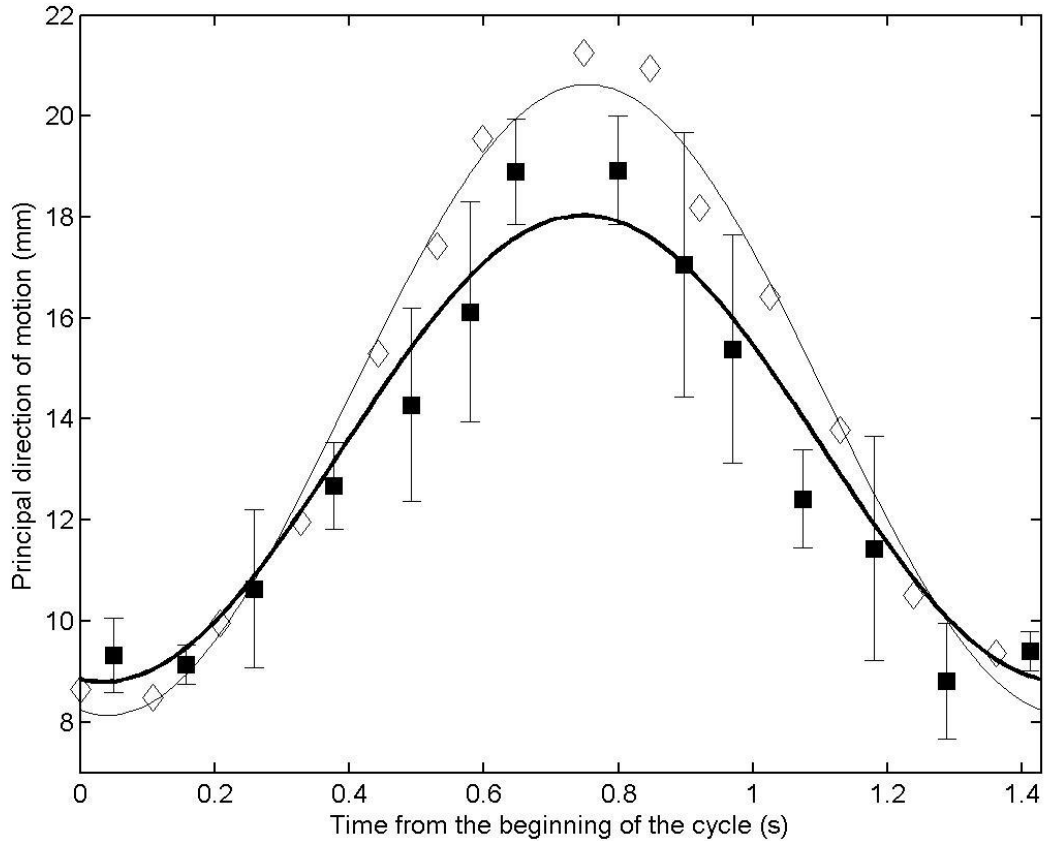


Fig. 6. Marker position (along the principal direction of motion) throughout the cardiac cycle. The position in the optical image is depicted with diamonds, while in the virtual image – squares. The analytical fits (lines) were used in the analysis of the spatial and timing accuracy.

The errors in time synchronization and the spatial shift between the optical and virtual images were quantified based on the screen coordinates of a fiducial marker placed on the surface of the phantom (Figure 5). The errors were expressed in terms of the projected errors. The overlap of the optical and virtual projected error vectors was analyzed with respect to the time elapsed from the cycle start, (Figure 6). The projected error vectors of both the optical and the virtual fiducial are expressed in terms of the coordinate along the principal direction of oscillation of the optical fiducial (considered as the reference). Each virtual data point was shifted right by 0.05 s to display the points at the average viewing instant, rather than when the program started displaying the corresponding virtual image. Cosine functions with the period $T = 1.428$ s (derived from the heart rate of 42 bpm) were fitted independently to the optical and the virtual data points:

$$y = A \cos(2\pi/T (t - t_0)) + B \quad (2)$$

The time lag t_0 (measured from the ECG synchronization signal) of displaying the optical (0.04 ± 0.02 s) or the virtual sequence (0.03 ± 0.04 s) is small compared to the interval between consecutive heart phases of 0.11 s. The phase difference between the two cosines (0.01 ± 0.05 s that constitutes 0.7 % of the motion period) represents the error in the synchronization of the display of the optical and the virtual images.

The absolute value of the difference in the amplitude shift B between the optical and the virtual cosines is small compared to the amplitude A ($1 \text{ mm} \ll 6.2 \text{ mm}$). The amplitude A of the virtual cosine is smaller by 25 % with respect to the amplitude of the optical cosine. The maximum difference between the cosines varies from -2.6 mm to 0.8 mm . This relatively large difference is partially caused by limitations in the reconstruction of the virtual images from the dynamic CT scan: each image is the average of 7 % of the cycle, and averaging around the minimum or the maximum values of the curve “flattens-out” the peaks. Also the images were not reconstructed between 49 % and 51 % of the cycle, resulting in additional “flattening” of the curve around 0.75 s from the beginning of the cycle.

4. DISCUSSION

The accuracy of the overlay achieved with the phantom system is close to our target value of 1 mm. The tracking accuracy is the primary source of error, and this will have to be addressed in the future. The large number of steps required to construct the virtual scene also results in accumulation of some error.

This research represents only a preliminary stage of the project, and provides a demonstration of a “proof of concept” for fusing dynamic endoscopic and virtual images of a beating heart phantom. The next phase of image fusion will involve validation using an in-vivo porcine model.

While we have demonstrated the applicability of this approach in laboratory settings, its adaptation to the clinical environment will present a number of challenges. A different organ tracking needs to be utilized, since optical tracking cannot be used in the closed chest. We plan to track the heart within the thorax using intra-operative angiogram data, as well as employing tracked trans-esophageal ultrasound, combined with the image-based registration approach proposed by Mori *et al.* [21].

The phantom motion (inflating/deflating movement following a cosine time dependence) is determined by the characteristics of the commercially available heart/thorax phantom we are using, and does not accurately reflect the dynamics of a real heart. The more complex time dependence of the motion of the human heart will necessitate more reconstructed phases of the heart motion, or non-uniform time interval between them.

The system operates in near-real time (14 images per second), due to limitations imposed by the currently available speed of the graphics system, and the complexity of the rendered virtual model.

5. CONCLUSIONS

We have demonstrated an accurate overlay of optical endoscopic images of a beating heart phantom with virtual equivalents generated based on dynamic 3D-CT data. High-quality animation of the virtual model was achieved through warping the static CT image of the diastolic phase to the CT images of other phases of the cardiac cycle. The image overlay is accurate within -0.8 mm and $+2.6 \text{ mm}$, with time synchronization error determined by the frame rate.

Acknowledgements.

The authors would like to thank Dr. D. Gobbi, R. Gupta, A. So, Dr. M. Drangova, C. Norley and C. Nikolov for assistance in various phases of this work. This research was supported by grant NA4755 from the Ontario Heart and Stroke Foundation, R3146-A02 from The National Science and Engineering Research Council of Canada, and by funding from the Ontario Consortium for Image-guided Therapy and Surgery (OCITS).

REFERENCES

1. W. Reynolds Jr., “The first laparoscopic cholecystectomy”, *J Soc. Laparoendosc. Surg.* 5:89-94 (2001).
2. E. R. Stephenson Jr, S. Sankholkar, C. T. Ducko, and R. J. Damiano Jr, “Successful endoscopic coronary artery bypass grafting: an acute large animal trial”, *J. Thorac. Cardiovasc. Surg.* 116:1071-3 (1998).
3. D. Loulmet, A. Carpentier, N. d’Attellis, A. Berrebi, C. Cardon, O. Ponzio, B. Aupècle, J. Y. M. Relland, “Endoscopic coronary artery bypass grafting with the aid of robotic assisted instruments”, *J. Thorac. Cardiovasc. Surg.* 118:4-10 (1999).

4. F. W. Mohr, V. Falk, A. Diegeler, and R. Autschbach, "Computer-enhanced coronary artery bypass surgery", *J. Thorac Cardiovasc Surg*, 117:1212-5 (1999).
5. B. Kiaii, W. D. Boyd, R. Rayman, W.D. Dobrowski, S. Ganapathy, G. Jablonsky, R.J. Novick, "Closed chest coronary surgery: preliminary experience using a harmonic scalpel and ZEUS", *The Heart Surgery Forum*, Vol. 3(3), pp 194-197 (2000).
6. G. Czibik, G. D'Ancona, H. W. Donias and H. L. Karamanoukian, "Robotic cardiac surgery: present and future applications", *J. Cardiothoracic Vasc. Anesthesia*, Vol 16, No 4, pp 495-501 (2002).
7. D. J. Vining, K. Liu, R. H. Choplin, E. F. Haponik, "Virtual bronchoscopy: relationships of virtual reality endobronchial simulations to actual bronchoscopic findings", *Chest*, vol. 109, pp.549-553 (1996).
8. H. Gulbins, H. Reichensperner, C. Becker, D. Boehm, A. Knez, C. Schmitz, R. Bruening, R. Haberl, and B. Reichart, "Preoperative 3D-reconstructions of ultrafast-CT images for the planning of minimally invasive direct coronary artery bypass operation (MIDCAB)", *Heart Surgery Forum*, 1, 111-115 (1998).
9. A. M. Chiu, D. Dey, M. Drangova, W. D. Boyd and T. Peters, "3-D image guidance for minimally invasive robotic coronary artery bypass (MIRCAB)", *Heart Surgery Forum*, 3(3): 224-231 (2000).
10. G. Lehmann, A. Chiu, D. Gobbi, Y. Starveld, D. Boyd, M. Drangova, T. Peters, "Towards dynamic planning of minimally invasive robotic cardiac bypass surgical procedures", *MICCAI 2001: LNCS 2208*, W. Nieslen and M. Viergever (eds), 368-375.
11. G. Lehmann, D. Habets, D.W. Holdsworth, T.M. Peters, M. Drangova, "Simulation of intra-operative 3D coronary angiography for enhanced minimally invasive robotic cardiac intervention", *MICCAI 2002(2): LNCS 2489*, T. Dohi and R. Kikinis (eds), 268-275.
12. D. Dey, D.G. Gobbi, P.J. Slomka, K.J.M. Surry, T.M. Peters, "Automatic fusion of freehand endoscopic brain images to three-dimensional surfaces: creating stereoscopic panoramas", *IEEE Trans Med Imaging* 21(1), 23-30 (2002).
13. R. Shahidi, M.R. Bax, C.R. Maurer, J.A. Johnson, E.P. Wilkinson, B. Wang, J.B. West, M.J. Citardi, K. H. Manwaring, R. Khadem, "Implementation, calibration and accuracy testing of an image-enhanced endoscopy system", *IEEE Trans Med Imaging* 21(12), 1524-1535 (2002).
14. F. Mourgues, T. Vieville, V. Falk, and È. Coste-Manière, "Interactive guidance by image overlay in robot assisted coronary artery bypass", *MICCAI 2003(1): LNCS 2878*, R. Ellis and T. Peters (eds), 173-181.
15. S. Szpala, G. Guiraudon, T. Peters, "Cardiac endoscopy enhanced by dynamic organ modeling for minimally-invasive surgery guidance", *MICCAI 2003(1): LNCS 2878*, R. Ellis and T. Peters (eds), 499-506.
16. L. Adhami and È. Coste-Maniere, "A versatile system for computer integrated mini-invasive robotic surgery", *MICCAI 2002: LNCS 2488*, T. Dohi and R. Kikinis (eds), 272-281.
17. J. Neider, T. Davis, and M. Woo, "OpenGL Programming Guide", Addison-Wesley, Menlo Park (1993).
18. M. Wierzbicki and T. Peters, "Determining epicardial surface motion using elastic registration: towards virtual reality guidance of minimally invasive cardiac intervention", *MICCAI 2003(1): LNCS 2878*, R. Ellis and T. Peters (eds), 722-729.
19. J. A. Nelder, R. Mead, "A simplex method for function minimization". *Computer Journal* 7, pp. 308-313 (1965).
20. D. Ruckert, L. I. Sonoda, C. Hayes, D.L.G. Hill, M.O. Leach, D.J. Hawkes, "Nonrigid registration using free-form deformations: application to breast MR images", *IEEE Trans Med Imaging* 18 (8), pp. 712-721 (1999).
21. K. Mori, D. Deguchi, J. Sugiyama, Y. Suenaga, J. Toriwaki, C.R. Maurer, H. Takabatake, H. Natori, "Tracking of a bronchoscope using epipolar geometry analysis and intensity-based image registration of real and virtual endoscopic images", *Med Image Anal* 6(3), 321-36 (2002).